

Suppression of magnetoresistance in thin WTe₂ flakes by surface oxidation

J. M. Woods^{1,2, ‡}, J. Shen^{1,2,+, ‡}, P. Kumaravadivel^{1,2}, Y. Pang³, Y. Xie^{1,2,4}, G. A. Pan⁵, M. Li⁶, E. I. Altman^{4,7}, L. Lu³, J. J. Cha^{1,2,4,}*

¹ Department of Mechanical Engineering and Materials Science, Yale University, New Haven, CT 06511, USA

² Energy Sciences Institute, Yale West Campus, West Haven, CT 06516, USA

³ Institute of Physics, Chinese Academy of Sciences, Beijing, China

⁴ Center for Research on Interface Structures and Phenomena, Yale University, New Haven, CT 06511, USA

⁵ Department of Physics, Yale University, New Haven, CT 06511, USA

⁶ Materials Characterization Core, Yale West Campus, West Haven, CT 06516, USA

⁷ Department of Chemical & Environmental Engineering, Yale University, New Haven, CT 06520, USA

⁺ present address: J.Shen-1@tudelft.nl

‡These authors contributed equally to this work.

RECEIVED DATE:

CORRESPONDING AUTHOR FOOTNOTE:

*Corresponding author. E-mail: judy.cha@yale.edu

Telephone number: +1 (203) 737-7293, Fax number: (203) 432-6775

Abstract:

Recent renewed interest in layered transition metal dichalcogenides stems from the exotic electronic phases predicted and observed in the single- and few-layer limit. Realizing these electronic phases requires preserving the desired transport properties down to a monolayer, which is challenging. Here, using semimetallic WTe₂ that exhibits large magnetoresistance, we show that surface oxidation and Fermi level pinning degrade the transport properties of thin WTe₂ flakes significantly. With decreasing WTe₂ flake thickness, we observe a dramatic suppression of the large magnetoresistance. This is explained by fitting a two-band model to the transport data, which shows that mobility of the electron and hole carriers decreases significantly for thin flakes. The microscopic origin of this mobility decrease is attributed to a ~ 2 nm-thick amorphous surface oxide layer that introduces disorder. The oxide layer also shifts the Fermi level by ~ 300 meV at the WTe₂ surface. However, band bending due to this Fermi level shift is not the dominant cause for the suppression of magnetoresistance as the electron and hole carrier densities

are balanced down to ~ 13 nm based on the two-band model. Our study highlights the critical need to investigate often unanticipated and sometimes unavoidable extrinsic surface effects on the transport properties of layered dichalcogenides and other 2D materials.

Keywords:

2D Layered Materials, Large Magnetoresistance, WTe₂, Electronic Transport, Fermi Level Pinning

Main Text:

Exotic electronic phases found in layered transition metal dichalcogenides (TMDCs), such as charge density waves,¹⁻³ topological surface states,⁴ and 2D superconductivity,^{2, 5} make TMDCs promising for a wide range of novel thin film electronics. In the single layer limit, additional electronic phases such as the quantum spin Hall state⁶ are predicted, which can be harnessed for spintronic and low-dissipation electronic applications. Recent progress in the ability to build heterostructures by stacking chalcogenide single layers with different electronic phases offers exciting opportunities for realizing interface- and proximity-induced electronic phases not possible in bulk forms.⁷ However, a critical requirement for device applications is to retain these predicted electronic phases and transport properties in the single layer limit. Often, this is not the case, as demonstrated by the presence of a 2D electron gas with low mobility at the surface of topological insulators such as Bi₂Se₃ and by surface oxidation of many 2D materials.⁸⁻¹⁰ Encapsulating layered

materials using boron nitride can be effective in preserving transport properties as shown for graphene,^{11, 12} but is still limited to individual nanoscale devices. Systematic studies of thickness-dependent transport properties of TMDCs are crucial for implementing practical applications based on these materials.

Among the TMDCs WTe₂ is a candidate for a type II Weyl semimetal¹³ and has recently received much attention largely due to its non-saturating large magnetoresistance (MR).¹⁴ This large MR has been ascribed to the near perfect electron and hole charge compensation,¹⁴ further supported by band structure calculations,¹⁵ angle-resolved photoemission spectroscopy (ARPES) measurements,¹⁶ and analysis of Shubnikov-de Hass oscillations.¹⁷⁻¹⁹ A classical two-band model is sufficient to describe the observed large MR despite the fact that the actual band structures are more complicated with four Fermi pockets along the Γ -X axis in the 1st Brillouin zone.^{19, 20} In addition, monolayer WTe₂ in the 1T' phase is predicted to exhibit the quantum spin Hall effect.⁶ Further theoretical calculation of layered WTe₂ predicts that the extremely large MR, and therefore the near-perfect charge compensation and high mobility, should be preserved down to the monolayer limit.¹⁵ The actual preservation of these electronic properties for fabricated devices of monolayer WTe₂ is vital in harnessing the exotic transport behavior⁶.

In contrast to these theoretical predictions, here we show that the MR of thin, mechanically exfoliated WTe₂ flakes decreases significantly compared to that of a bulk crystal. This is in agreement with the recent report by L. Wang *et al.*,²¹ which also showed

dramatic suppression of the MR in WTe₂ thin flakes down to 6 layers. The suppression of the MR was attributed to decreased mobility and increased disorder due to surface degradation but a microscopic origin was not investigated. Here, we reveal the microscopic origin for MR suppression by correlating transport measurements with the microstructure of WTe₂ flakes from 145 nm down to 2.5 nm (~ 3 layers). We find that the microscopic source is a ~ 2 nm amorphous surface oxide layer. The work function of the oxide layer is found to be ~ 300 meV less than that of clean WTe₂, suggesting a potential charge imbalance between the electron and hole carriers of WTe₂ at the WTe₂ surface due to downward band bending by the Fermi level pinning, which would lead to suppression of MR. However, due to the limited spatial extent of the band bending, estimated to be ~ 1 nm by Poisson's equation, the Fermi level pinning is not the dominant cause behind the degradation of MR. A much larger factor is the increased disorder induced by the surface oxide layer, reflected in the transport data as a decrease in mobility and weak anti-localization.

Electronic transport measurements of WTe₂ thin flakes, mechanically exfoliated from bulk crystals (Supporting Information Figure S1-3), were taken from 300 K to 2 K with magnetic fields up to 9 T. Figure 1(a)-(e) show the temperature-dependent longitudinal resistance, $R_{xx}(T)$, with and without a 9 T magnetic field perpendicularly applied to the basal plane of WTe₂. In the absence of a magnetic field, $R_{xx}(T)$ shows the expected semi-metallic behavior with the residual resistance ratio (RRR) defined as $R_{xx}(300K)/R_{xx}(1.8K)$. When field-cooled at 9 T, R_{xx} increases at low temperature due to the emergence of the large MR, with T_{on} defined as the temperature at which R_{xx} starts to increase. Both T_{on} and

RRR start to decrease significantly for flakes thinner than ~ 40 nm (Figure 1(f)). Figure 1(g)-(k) show the corresponding MR curves measured at 1.8 K with MR defined as $[R(B)-R(0)]/R(0)$. With decreasing WTe_2 thickness, MR decreases linearly (Figure 1(l)). These observations clearly indicate that the transport properties of WTe_2 degrade with decreasing WTe_2 thickness.

Strong correlations between the crystal quality and MR^{22} as well as the carrier doping and the MR^{23} have been shown using WTe_2 bulk crystals. Thus, the observed MR suppression suggests either degradation of crystal quality or changes in transport property such as the carrier density and mobility for thin WTe_2 flakes. We measure the Hall resistance $R_{xy}(B)$ of the flakes from 145 nm down to 2.5 nm to find the origin of the MR suppression (Figure 2 and Figure S4). For all thicknesses, strong non-linearity is observed in R_{xy} , suggesting that at least two carrier types contribute to the Hall curves. In WTe_2 the Fermi level cuts through the conduction and valence bands,¹⁴ so both electron and hole carriers are expected to contribute to transport. Therefore, we use the classical two-band model for resistivity (ρ_{xx} and ρ_{xy} in equation (1)²⁴) to fit the R_{xx} and R_{xy} curves, with the appropriate geometrical factors considered, assigning one band to electrons and the other to holes. Supporting Information Figure S5 shows the fitted curves, which overlap well with the measured data down to the 13 nm flake.

$$\begin{cases} \rho_{xy} = \frac{(n_h\mu_h^2 - n_e\mu_e^2)B + \mu_h^2\mu_e^2(n_h - n_e)B^3}{e[(n_h\mu_h + n_e\mu_e)^2 + (n_h - n_e)^2\mu_h^2\mu_e^2B^2]} \\ \rho_{xx} = \frac{(n_h\mu_h + n_e\mu_e) + (n_h\mu_h\mu_e^2 + n_e\mu_e\mu_h^2)B^2}{e[(n_h\mu_h + n_e\mu_e)^2 + (n_h - n_e)^2\mu_h^2\mu_e^2B^2]} \end{cases} \quad (1)$$

Figure 2(f) shows the electron and hole carrier densities, n_e and n_h , obtained from the fit as a function of WTe₂ thickness. Figure 2(g) shows the corresponding mobility values, μ_e and μ_h . Figure 2(h) shows the charge carrier density ratio, n_e/n_h . We see that as thickness decreases the mobility and the total charge concentration decrease, but the ratio of the electron to hole densities remains close to one down to 13 nm. The two-band model does not describe well the transport data of the 6.3 nm and 2.5 nm flakes because of the weak anti-localization that starts to dominate in these thin flakes (Figure 1(k) and Figure S5(j)). Temperature-dependent MR and Hall studies for 115 nm and 13 nm WTe₂ flakes are shown in Figure S6. Based on the fit results using the two-band model, we attribute the suppression of MR with decreasing WTe₂ flake thickness (Figure 1(l)) to the decrease in electron and hole mobility values, and not to the charge imbalance as the electron and hole carrier densities are nearly equal down to the 13 nm WTe₂ flake.

The dramatic decrease in the mobility values suggests presence of a 2D impurity band with very low mobility that induces strong scatter in thin flakes. The effect of the 2D impurity band to the transport properties of WTe₂ thin flakes is studied by analyzing Shubnikov-de Hass (SdH) oscillations as a function of WTe₂ flake thickness. Figure 3(a) shows $R_{xx}(B)$ plotted in B^2 , which clearly shows the quadratic dependence of MR on B , as expected from Equation (1) for ρ_{xx} when $n_h \approx n_e$, and also shows the suppression of MR with decreasing thickness. From the second derivative of $R_{xx}(B)$, d^2R_{xx}/dB^2 (Figure 3(b)), SdH oscillations are observed down to the 13 nm thick sample, indicating the presence of high mobility carriers. More importantly, the field B_Q at which the SdH oscillations start to emerge remains constant at ~ 4.7 T for all thicknesses down to 13 nm. Using the

condition $\mu_{SDH} \cdot B \sim 1$ we obtain a constant mobility for the high mobility carriers. This is in contrast to the decreasing electron and hole mobilities obtained from the Hall curves (Figure 2(g)). The average mobility obtained from the Lorentz law, $MR \approx (\mu_{avg} B)^2$, is plotted together with μ_{SDH} , for comparison, as a function of WTe₂ thickness (Figure 3(c)). The systematic decrease in μ_{avg} suggests increased scattering in thinner WTe₂ flakes due to the 2D impurity band near the surface. The constant μ_{SDH} suggests that the 2D impurity band does not scatter the high mobility carriers down to 13 nm. The role of the 2D impurity band on μ_{avg} is further substantiated from the change in conductivity (and corresponding resistivity) with decreasing thickness (Figure 3(d)).

To reveal the microscopic origin of the 2D impurity band, we examine a WTe₂ flake by cross-sectional transmission electron microscopy (TEM), energy dispersive X-ray spectroscopy (EDX), and X-ray photoelectron spectroscopy (XPS). Figure 4(a) shows the cross-sectional TEM image of a WTe₂ flake transferred onto a SiO₂/Si substrate, in which WTe₂ layers are clearly resolved (dotted red box). Below the crystalline WTe₂, we observe two different amorphous layers with a distinct contrast in intensity. The bottom layer of lighter contrast corresponds to the SiO₂ substrate, confirmed by EDX. Chemical analysis of the darker amorphous layer (dotted green box) indicates the presence of oxygen, tellurium, and tungsten (Figure 4(b)), whereas the oxygen peak is absent in the crystalline WTe₂ region. Thus, we conclude that a ~ 2 nm thick oxide layer forms on WTe₂ flakes. Oxide formation can be detected within a few hours by comparing XPS spectra of WTe₂ flakes, freshly cleaved/cleaned and after being left in air for 3.5 hours (Figure 4(c,d)). The clean WTe₂ flakes were obtained by sputtering the surface of freshly cleaved WTe₂ flakes

for ~ 2 min with Ar at 5 keV, which completely removed the oxide layer. Pronounced W-O_x and Te-O_x peaks are observed after 3.5 hours in air, which were not present in the freshly cleaved and sputtered sample. The XPS data corroborates the observation that the amorphous layer observed in the cross-sectional TEM image is indeed a surface oxide of WTe₂.

The surface oxide layer induces disorder that manifests itself as a 2D impurity band with low mobility, leading to the suppression of MR for thinner flakes. In addition, the surface oxide layer can induce downward band bending near the surface of WTe₂ by pinning the Fermi level. This was measured by ultraviolet photoelectron spectroscopy (UPS). Figure 4(e) shows the secondary edge of clean (black) and air-exposed (red) WTe₂ flakes. After exposure to air, the secondary edge increases by about 300 meV, which indicates a corresponding decrease in the work function from 4.5 eV to 4.2 eV. For the WTe₂ near the surface oxide, the bands are bent (Figure 4(f)). Using Poisson's equation and the dielectric constant of WTe₂²⁵ we determine the spatial extent of the band bending to be about 1 nm. This limited spatial extent of the band bending explains why the charge compensation holds down to a 13 nm WTe₂ flake. Full UPS profiles and details of Poisson's equation calculations are shown in Figure S7. Additionally, the ~ 2 nm thick oxide layer induces strong disorder for very thin WTe₂ flakes so that a localization effect should be discernible. This is indeed the case for the ~ 3 layer WTe₂ flake where a pronounced weak antilocalization (WAL) signal is observed due to the induced disorder (Figure 1(k)). Moreover, WAL is expected due to the strong spin-orbit coupling in WTe₂. We fit the two-

dimensional Hikami-Larkin-Nagaoka localization model²⁶ to the observed WAL and obtain a B_ϕ of 0.074T for fixed B_{SO} above 3.5 T (Figure S8).

Transport degradation due to surface oxidation is a major issue that affects most of the transition metal dichalcogenide family and other 2D materials. In the topological insulators Bi_2Se_3 and Bi_2Te_3 , a disordered 2D gas at the surface complicates the analysis of the topological surface states.^{8, 9} In black phosphorus, which possesses high mobility and anisotropic optical properties due to its crystal structure, fast surface oxidation significantly degrades device performance.^{27, 28} Here, the observed degradation in transport properties of thin WTe_2 flakes is due to disorder induced by surface oxidation, leading to suppression of the large MR in WTe_2 . In addition, our finding suggests that the predicted quantum spin Hall state may not be observed in unprotected single layer WTe_2 unless an effective encapsulation layer such as boron nitride is used.

Methods

WTe₂ synthesis

WTe₂ crystals were grown by a chemical vapor transport (CVT) method. 0.55 g of a WTe₂ source (American Elements, 99.999%) and 80 mg of an I₂ transport agent were placed in a quartz tube sealed at one end. The tube was purged with argon gas multiple times, and sealed with a base pressure below 50 mTorr. The sealed quartz vessel was placed in a two zone furnace. Over the course of 6 hours, the ‘hot’ end with the source powder was ramped up to 950 °C and the ‘cold’ end was ramped up to 800 °C. The furnace was held at these temperatures for 3 days. Upon cooling, WTe₂ crystals formed at the ‘cold’ end of the tube. These bulk crystals were then mechanically exfoliated on 285 nm SiO₂/Si substrates using the standard tape method to obtain thin WTe₂ flakes.

Device fabrication and transport measurements

Devices were fabricated by standard e-beam lithography using a Vistec EBPG 5000+. 5/200 nm thick Cr/Au electrical contacts were deposited by thermal evaporation (MBraun MB-EcoVap). The low temperature and magnetic field transport measurements were performed soon after the lift-off process, using a Quantum Design Dynacool physical property measurement system equipped with a 9 T magnet and at a base temperature of 1.8 K. The thickness of the WTe₂ flakes was measured by a Bruker Fastscan AFM directly after the transport measurements to minimize the exposure of flakes to air.

Structure characterizations

The morphology and chemical composition were characterized by TEM/STEM (FEI Technai Osiris200kV). Cross-sectional TEM samples were prepared by focused ion beam (Zeiss Crossbeam 540) at Carl Zeiss Microscopy, LLC. Planar samples were obtained by sonicating WTe₂ flakes in methanol and drop-casting onto a TEM grid.

XPS and UPS (He I illumination, E=21.22eV) measurements (PHI 5000 Versa Probe II) were conducted to determine the chemical and electrical nature of WTe₂ before and after exposure to air. For clean WTe₂ flakes for the UPS measurements, the freshly cleaved flakes were sputtered for ~2 minutes using an Ar source at 4 keV.

ASSOCIATED CONTENT

Supporting Information.

The Supporting Information is available free of charge via the Internet at <http://pubs.acs.org>.

TEM characterization of WTe₂ crystal; Atomic force microscopy (AFM) and Raman characterizations of exfoliated WTe₂ flakes; X-ray diffraction pattern (XRD) of exfoliated WTe₂ flakes; Transport data ($R_{xx}(T)$, MR, and Hall) for two more thicknesses, 13 nm and 60 nm; Least square fit using the two-band model for Hall and MR curves in Figure 2; Temperature-dependent MRs and Hall curves, as well as the fitting result for the thick sample (115nm) and thin sample (13nm); Full UPS profiles of clean and 3.5 hours air-exposed WTe₂; 2D WAL for the ~ 2.5 nm sample.

AUTHOR INFORMATION

Corresponding Author

*E-mail: judy.cha@yale.edu.

Present Addresses

⁺ (J. S.) University of Delft, Netherlands, J.Shen-1@tudelft.nl

Author Contributions

The manuscript was written through contributions of all authors. All authors have given approval to the final version of the manuscript. ‡J. M. W. and J. S. contributed equally.

Acknowledgements

This work was supported by Department of Energy, Basic Energy Science, Award No. DE-SC0014476. J. S. was partially supported by NSF DMR 1402600. J. M. W. was partially supported by NSF EFMA 1542815. P.K. was supported by DOE DE-SC0014476. Characterization facilities used in this work were supported by the Yale Institute for Nanoscience and Quantum Engineering (YINQE), MRSEC DMR 1119826, and Yale West Campus Materials Characterization Core. Raman characterization was conducted at the Yale Institute for the Preservation of Cultural Heritage.

References

1. Xi, X.; Zhao, L.; Wang, Z.; Berger, H.; Forró, L.; Shan, J.; Mak, K. F. *Nat. Nano.* **2015**, 10 (9), 765-769.
2. Ugeda, M. M.; Bradley, A. J.; Zhang, Y.; Onishi, S.; Chen, Y.; Ruan, W.; Ojeda-Aristizabal, C.; Ryu, H.; Edmonds, M. T.; Tsai, H.-Z.; Riss, A.; Mo, S.-K.; Lee, D.; Zettl, A.; Hussain, Z.; Shen, Z.-X.; Crommie, M. F. *Nat. Phys.* **2016**, 12 (1), 92-97.
3. Li, L. J.; O'Farrell, E. C. T.; Loh, K. P.; Eda, G.; Özyilmaz, B.; Castro Neto, A. H. *Nature* **2016**, 529 (7585), 185-189.
4. Xia, Y.; Qian, D.; Hsieh, D.; Wray, L.; Pal, A.; Lin, H.; Bansil, A.; Grauer, D.; Hor, Y. S.; Cava, R. J.; Hasan, M. Z. *Nat. Phys.* **2009**, 5 (6), 398-402.
5. Tsen, A. W.; Hunt, B.; Kim, Y. D.; Yuan, Z. J.; Jia, S.; Cava, R. J.; Hone, J.; Kim, P.; Dean, C. R.; Pasupathy, A. N. *Nat. Phys.* **2015**, advance online publication.
6. Qian, X.; Liu, J.; Fu, L.; Li, J. *Science* **2014**, 346 (6215), 1344-1347.
7. Geim, A. K.; Grigorieva, I. V. *Nature* **2013**, 499 (7459), 419-425.
8. Bianchi, M.; Guan, D.; Bao, S.; Mi, J.; Iversen, B. B.; King, P. D. C.; Hofmann, P. *Nat. Commun.* **2010**, 1, 128.
9. Kong, D.; Cha, J. J.; Lai, K.; Peng, H.; Analytis, J. G.; Meister, S.; Chen, Y.; Zhang, H.-J.; Fisher, I. R.; Shen, Z.-X.; Cui, Y. *ACS Nano* **2011**, 5 (6), 4698-4703.
10. Jung, Y.; Shen, J.; Cha, J. J. *Nano Convergence* **2014**, 1 (1), 1-8.
11. Mayorov, A. S.; Gorbachev, R. V.; Morozov, S. V.; Britnell, L.; Jalil, R.; Ponomarenko, L. A.; Blake, P.; Novoselov, K. S.; Watanabe, K.; Taniguchi, T.; Geim, A. K. *Nano Letters* **2011**, 11 (6), 2396-2399.
12. Wang, L.; Meric, I.; Huang, P. Y.; Gao, Q.; Gao, Y.; Tran, H.; Taniguchi, T.; Watanabe, K.; Campos, L. M.; Muller, D. a.; Guo, J.; Kim, P.; Hone, J.; Shepard, K. L.; Dean, C. R. *Science* **2013**, 342, 614-617.
13. Soluyanov, A. A.; Gresch, D.; Wang, Z.; Wu, Q.; Troyer, M.; Dai, X.; Bernevig, B. A. *Nature* **2015**, 527 (7579), 495-498.
14. Ali, M. N.; Xiong, J.; Flynn, S.; Tao, J.; Gibson, Q. D.; Schoop, L. M.; Liang, T.; Haldolaarachchige, N.; Hirschberger, M.; Ong, N. P.; Cava, R. J. *Nature* **2014**, 514 (7521), 205-208.
15. Lv, H. Y.; Lu, W. J.; Shao, D. F.; Liu, Y.; Tan, S. G.; Sun, Y. P. *Europhys. Lett.* **2015**, 110 (3), 37004.
16. Pletikosić, I.; Ali, M. N.; Fedorov, A. V.; Cava, R. J.; Valla, T. *Phys. Rev. Lett.* **2014**, 113 (21), 216601.
17. Cai, P. L.; Hu, J.; He, L. P.; Pan, J.; Hong, X. C.; Zhang, Z.; Zhang, J.; Wei, J.; Mao, Z. Q.; Li, S. Y. *Phys. Rev. Lett.* **2015**, 115 (5), 057202.
18. Rhodes, D.; Das, S.; Zhang, Q. R.; Zeng, B.; Pradhan, N. R.; Kikugawa, N.; Manousakis, E.; Balicas, L. *Phys. Rev. B* **2015**, 92 (12), 125152.
19. Zhu, Z.; Lin, X.; Liu, J.; Fauqué, B.; Tao, Q.; Yang, C.; Shi, Y.; Behnia, K. *Phys. Rev. Lett.* **2015**, 114 (17), 176601.
20. Jiang, J.; Tang, F.; Pan, X. C.; Liu, H. M.; Niu, X. H.; Wang, Y. X.; Xu, D. F.; Yang, H. F.; Xie, B. P.; Song, F. Q.; Dudin, P.; Kim, T. K.; Hoesch, M.; Das, P. K.; Vobornik, I.; Wan, X. G.; Feng, D. L. *Phys. Rev. Lett.* **2015**, 115 (16), 166601.
21. Wang, L.; Gutierrez-Lezama, I.; Barreteau, C.; Ubrig, N.; Giannini, E.; Morpurgo, A. F. *Nat. Commun.* **2015**, 6, 8892.

22. Mazhar, N. A.; Leslie, S.; Jun, X.; Steven, F.; Quinn, G.; Max, H.; Ong, N. P.; Cava, R. J. *Europhys. Lett.* **2015**, 110 (6), 67002.
23. S. Flynn; M. Ali; Cava, R. J. *arXiv:1506.07069* **2015**.
24. Murzin, S. S.; Dorozhkin, S. I.; Landwehr, G.; Gossard, A. C. *J. Exper. Theor. Phys. Lett.* 67 (2), 113-119.
25. Kumar, A.; Ahluwalia, P. K. *Physica B: Condens. Matter* **2012**, 407 (24), 4627-4634.
26. S. Hikami; A. I. Larkin; Nagaoka, Y. *Prof. Theor. Phys.* **1980**, 63, 707-710.
27. Favron, A.; Gaufres, E.; Fossard, F.; Phaneuf-Lheureux, A.-L.; Tang, N. Y. W.; Levesque, P. L.; Loiseau, A.; Leonelli, R.; Francoeur, S.; Martel, R. *Nat. Mater.* **2015**, 14 (8), 826-832.
28. He Tian *et al.* *arXiv: 1603.03988* **2016**.

Figures

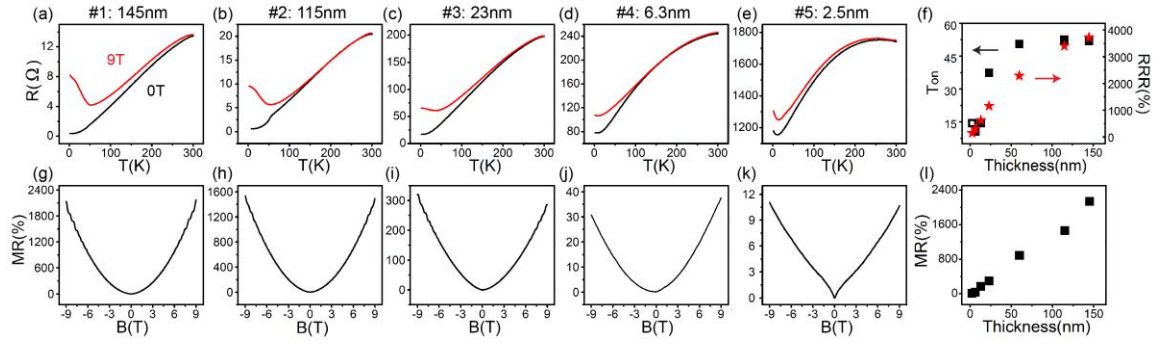


Figure 1 | Thickness dependent transport properties of WTe₂ films: T_{on} , RRR and MR .

(a)-(e) R-T curves at 0 T and 9 T for samples with different thicknesses. (f) The T_{on} and RRR extracted from these curves are plotted against thickness. We see that values for both T_{on} and RRR systematically decrease for decreasing thickness. (g)-(k) the corresponding MR curves of the samples on the upper panel at $T = 1.8$ K. MR at 9 T as a function of thickness is summarized in (l), mirroring the effects seen on T_{on} and RRR ; the magnitude of the MR decreases dramatically as thinner WTe₂ flakes are measured. For the thinnest flake (device #5, 2.5 nm thickness) WAL is observed in the resistance vs. magnetic field plot.

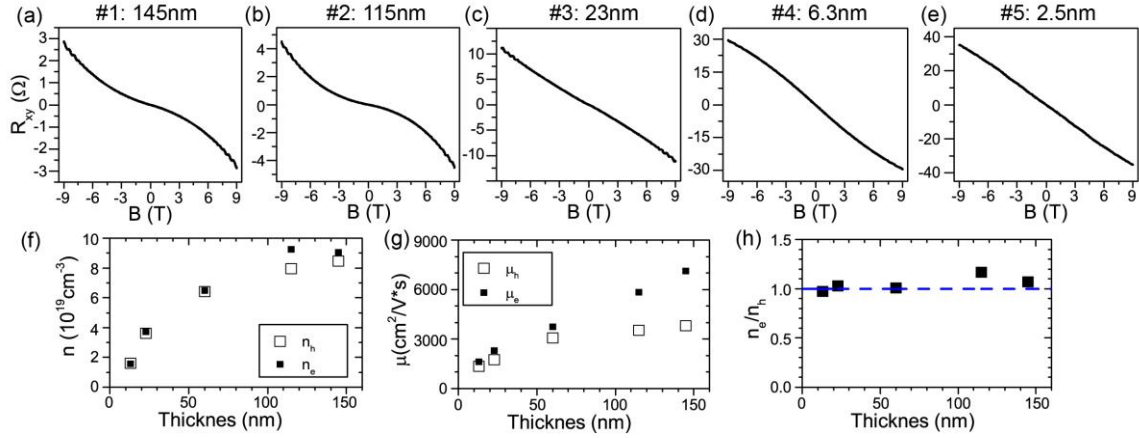


Figure 2 | Thickness dependent mobility and carrier density from a two-band model.

(a)-(e) Hall curves measured at 1.8 K for samples with different thicknesses. **(f)** The carrier densities and **(g)** mobilities of the electrons (solid squares) and holes (open squares) from the two band model fits of the Hall and MR curves summarized as a function of thickness down to 13 nm. Comparison of the data to the fit is shown in Figure S5. The fits for the 6.3 nm and 2.5 nm flakes are not shown due to the addition of WAL behavior in the R_{xx} data. **(h)** Ratio of the electron carrier density, n_e , to the hole carrier density, n_h , as a function of thickness. Carrier compensation holds down to the 13 nm flake.

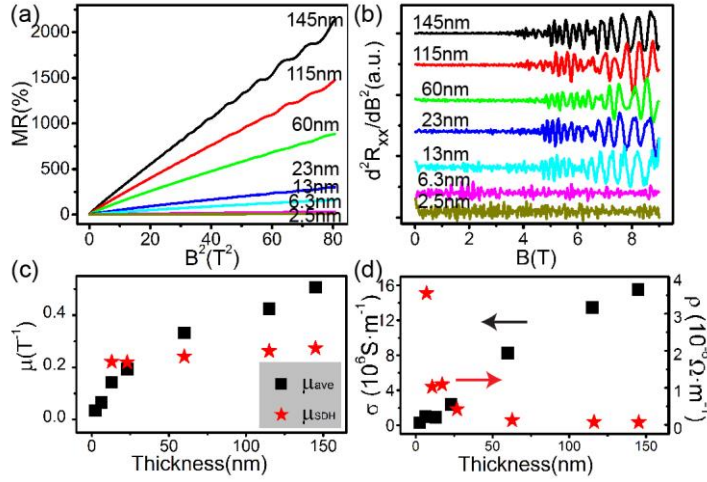


Figure 3 | MR versus B^2 and SdH oscillations for WTe₂ flakes of different thicknesses.

(a) MRs measured at $T = 1.8$ K plotted as a function of B^2 . The curves are linear as expected from the classical Lorentz law for MR. (b) SdH oscillations observed in samples thicker than 13nm disappear in thinner samples. (c) The average mobility calculated from MR (μ_{avg}) and the mobility of the fastest carriers calculated based on the onset of the SdH oscillations (μ_{SdH}) plotted together as a function of thickness. (d) The thickness dependence of the conductivity and resistivity of samples is consistent with that of μ_{avg} .

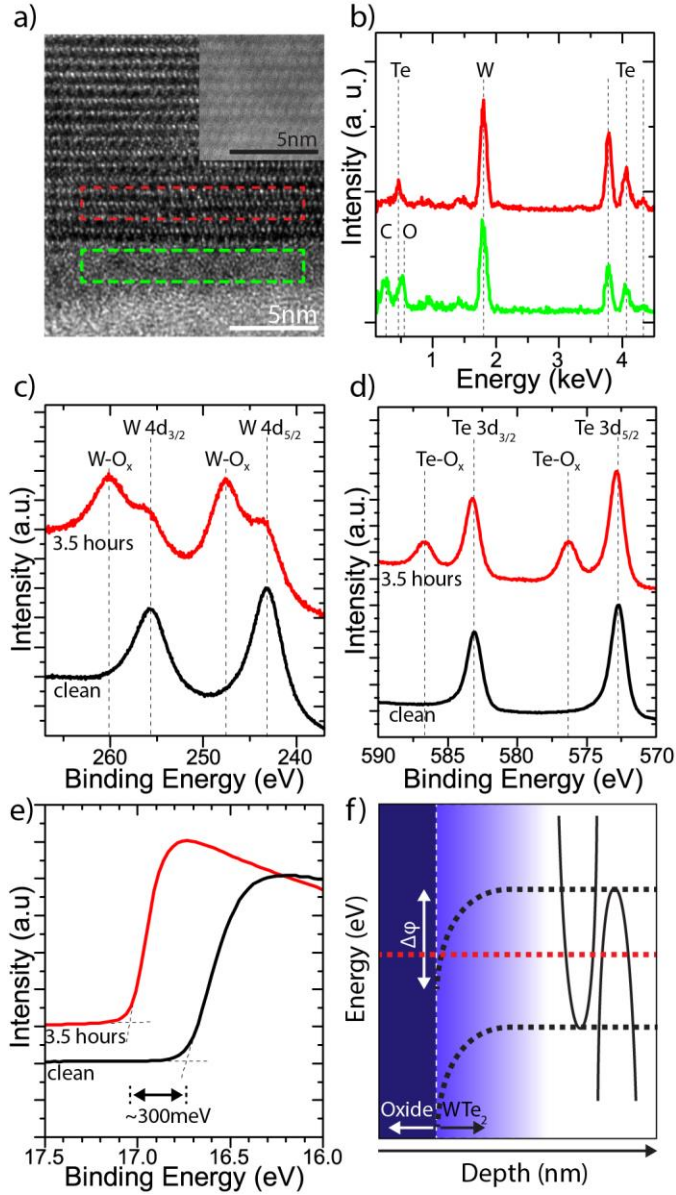


Figure 4 | STEM characterization, X-ray photoelectron spectroscopy (XPS) and ultraviolet photoelectron spectroscopy (UPS). (a) Cross-sectional TEM image of WTe₂. The inset shows the corresponding STEM annular dark field image. (b) EDX spectra of red and green dashed-line regions of (a). Oxygen is present only in the green region indicating this is an amorphous tungsten-tellurium oxide layer. This amorphous oxide layer is also present on the top surface of the flake. The bottom-most brighter amorphous layer is SiO₂

(c,d) XPS profiles for W (c) and Te (d) on clean flakes (black) and flakes with 3.5 hours of exposure to air (red). The presence of Te-O_x and W-O_x peaks after 3.5 hours of air exposure indicates formation of an oxide layer on the surface of the WTe₂ flakes. (e) UPS profiles of the secondary edge for clean (black) and 3.5 hours air exposed (red) WTe₂ flakes. The location of the secondary edge increases by about 300 meV, indicating a corresponding work function, ϕ , decrease of about 300 meV. (f) Schematic of Fermi level pinning between the surface oxide (left) and WTe₂ flake (right). The Fermi level is marked by a red dashed line. The Valence and conduction bands are shown on right. Black dashed lines track the location of the top/bottom of the valence/conduction bands in the proximity of the oxide interface.